Journal of Solid State Chemistry 283 (2020) 121139

Contents lists available at ScienceDirect

Journal of Solid State Chemistry

journal homepage: www.elsevier.com/locate/jssc

High-pressure responses of alkali metal hydrogen carbonates, $RbHCO_3$ and $CsHCO_3$: Findings of new phases and unique compressional behavior

Riko Iizuka-Oku *, Weibin Gui, Kazuki Komatsu, Takehiko Yagi, Hiroyuki Kagi

Geochemical Research Center, Graduate School of Science, The University of Tokyo, Tokyo, 113-0033, Japan

ARTICLE INFO

Keywords:
Hydrogen carbonate
Hydrogen bonding
High-pressure behavior
Phase transition
Alkali metal
In situ observation

ABSTRACT

High-pressure responses of $RbHCO_3$ and $CsHCO_3$ were characterized by *in situ* Raman spectroscopy and X-ray and neutron diffraction observations. $RbHCO_3$ exhibited a monoclinic (phase IV) and a triclinic (phase V) high-pressure phase at ~0.5 GPa and room temperature. Increasing compression induced unique behavior in a specific cell parameter (*a* in phase IV or *c* in phase V), which first increased, and then decreased at ~1 GPa, likely owing to the rearrangement of Rb^+ and reconfiguration of the ordered $(HCO_3^-)_2$ dimers. Deuterium positions in phase IV of $RbDCO_3$ were determined. The hydrogen bonding remained moderately strong, and possibly did not affect the phase transition despite the accompanying disordering and ordering of the dimers. $CsHCO_3$ showed no structural change up to 5 GPa, suggesting that its ambient phase (isostructural to phase IV of $KHCO_3$) was already stable at high pressure. The structural stability appeared to be systematically related to the cation size.

1. Introduction

Behaviors of some carbonates and hydrous minerals at high pressure are fundamentally important to geochemical systems and processes, such as the global carbon cycle, the evolution of the atmosphere, and water storage in the deep Earth. Carbonates and bicarbonates (hydrogen carbonates) act as sinks for carbon dioxide. There is increasing interest in these materials for use in the sequestration of CO_2 produced by the combustion of fossil fuels, and their locality and thermodynamic behaviors have been studied. Hydrogen carbonates are minor minerals, but they show interesting characteristic of hydrogen bonding that affects their phase stability. Therefore, the pressure responses of these materials have attracted much attention, not only in geoscience and biomineralogy, but also in physical chemistry.

Alkali metal hydrogen carbonates ($MHCO_3$, M = Na, K, Rb, and Cs) are a series of inorganic substances that contain HCO_3^- anions and alkali metal (elemental) cations. $NaHCO_3$ (nahcolite) has a structure consisting of infinite chains of HCO_3^- [1,2]. The other three hydrogen carbonates have HCO_3^- ions that form dimers connected by two hydrogen bonds. These dimers align parallel with each other to create the crystal structure, and the cations occupy the spaces between them. The ambient phase of $KHCO_3$ (phase II, monoclinic, $P2_1/a$) undergoes several transitions at high pressure or temperature. A temperature-induced phase transition at T_C = 318 K (351 K for $KDCO_3$) takes the ambient phase II to high-temperature (high-T) phase I (monoclinic, $C2/m$) [3]. At room temperature, $KHCO_3$ transforms at ~3 GPa [4–6], and there are two stable two high-pressure (high-P) phases, which are monoclinic phase IV ($P2_1$/b, non-standard setting of $P2_1/c$) reported by Komatsu et al. [7] and triclinic phase V ($P\overline{1}$) reported by Allan et al. [8]. These two high-P phases have been observed, either singly or together, under various experimental conditions using single-crystal X-ray diffraction (XRD) [7], single-crystal XRD, and powder neutron diffraction [8], and their abundance ratio varied with each experimental run. Takasaka et al. [9] reported another high-P phase (phase III, triclinic $C1$ or $C\overline{1}$) under high shear stress. The $(HCO_3^-)_2$ dimers were disordered only in the high-T phase I, and they were ordered in all other $KHCO_3$polymorphs. Table 1 summarizes the structural information for the $KHCO_3$ polymorphs, $RbHCO_3$, and $CsHCO_3$. The Roman numeral phase identifiers for $RbHCO_3$ and $CsHCO_3$ are first given in this study. Although phase III of $RbHCO_3$ has not yet been reported, the numeral is reserved in case of its discovery, which is considered highly likely. In contrast, the phases of $CsHCO_3$ are renumbered from I, because there is no guarantee of finding phases corresponding to phases I to III of $KHCO_3$ or $RbHCO_3$.

Under ambient conditions, $RbHCO_3$ and $CsHCO_3$ have $(HCO_3^-)_2$ dimer configurations, but take slightly different structures to $KHCO_3$ depending on pressure and temperature. The ambient phase of $RbHCO_3$ (phase I) is isostructural with $KHCO_3$ (phase I, $C2/m$), and has disordered hydrogen atoms. Larvor and Stöger [10] reported it transforms into an

* Corresponding author.
E-mail address: riizuka@eqchem.s.u-tokyo.ac.jp (R. Iizuka-Oku).

https://doi.org/10.1016/j.jssc.2019.121139
Received 27 September 2019; Received in revised form 14 December 2019; Accepted 17 December 2019
Available online 24 December 2019

Table 1
Summary of phases and corresponding structures of $KHCO_3$, $RbHCO_3$, and $CsHCO_3$.

crystal system	monoclinic	monoclinic	triclinic	monoclinic	triclinic
dimer configuration					
$KHCO_3$	disordered **I**	ordered (anti-phase) **II**	ordered (in-phase) **III**	ordered (anti-phase) **IV**	ordered (in-phase) **V**
$RbHCO_3$[a]	high-T > 318K Ref. [3] **I**	low-T (ambient) Ref. [3] **II**	shear-stress-induced Ref. [9] **III**	high-P > 2.8 GPa Refs. [4–7] **IV**	high-P > 3.2 GPa Ref. [8] **V**
$CsHCO_3$[a]	high-T (ambient) Ref. [10]	low-T < 245K Ref. [10]	Undiscovered	high-P > ~0.5 GPa This study **I** ambient Ref. [11]	high-P > ~0.5 GPa This study

[a] Phase numbers for $RbHCO_3$ and $CsHCO_3$ are first given in this study. See details in text.

ordered phase (*C*1) at low temperature (below 245 K). The structure of $CsHCO_3$ [11] (designated here as $CsHCO_3$ phase I, Table 1) is equivalent to the high-P phase IV of $KHCO_3$, although the positions of the hydrogen atoms remain unclear [7]. Therefore, systematic changes in the phase relations may be possible in $MHCO_3$ hydrogen carbonates, where M = K, Rb, and Cs. Pressure-induced phase transitions generally follow patterns in isostructural compounds depending on the cation size (e.g., alkali metal chlorides MCl, M = Na, K, Rb, and Cs). However, no high-P behavior has been reported for the hydrogen carbonates $RbHCO_3$ and $CsHCO_3$. Any trends in the series should be clarified to improve understanding of the behavior of hydrogen bonding in these crystal structures under high pressure.

In the present study, the high-P behaviors of $RbHCO_3$ and $CsHCO_3$ were investigated via *in situ* studies using Raman spectroscopy, powder XRD, and neutron diffraction. The phase relations, hydrogen bonding configuration, and its stability in the structures are discussed.

2. Experimental methods

2.1. Sample syntheses

$CsHCO_3$ was obtained commercially from Wako Pure Chemical Industries, Ltd. (purity 99%). $RbHCO_3$ and $RbDCO_3$ were synthesized from Rb_2CO_3 (purity 99% (2 N), Kojundo Chemical Laboratory Co., Ltd.) in our laboratory. All synthesized samples were identified as well-crystallized powders from powder XRD patterns (MiniFlex II, Rigaku; 30 kV, 15 mA, Cu*K*α) and Raman spectra (see later in Section 2.3).

2.1.1. $RbHCO_3$

Powdered $RbHCO_3$ was synthesized by the reaction $Rb_2CO_3 + H_2O + CO_2 \rightarrow 2RbHCO_3$. Using the difference in aqueous solubility between Rb_2CO_3 (223 g/100 g water at 20 °C) and $RbHCO_3$ (116 g/100 g water at 20 °C) [12], $RbHCO_3$ crystals were precipitated from a water–ethanol solution. Rb_2CO_3 (2 g) was placed in a beaker to which was added ethanol (100 mL). Pure water (milli-Q; Nihon Millipore Ltd.) was injected dropwise with a syringe until the Rb_2CO_3 crystals dissolved completely. The mixed solution was filtered through a funnel to remove undissolved reagents. CO_2 was bubbled into the mixed solution for several hours until the amount of crystals did not obviously increase. The solution was vacuum filtered, and the crystalline powder was dried and kept in a vacuum desiccator to avoid absorbing atmospheric moisture.

2.1.2. $RbDCO_3$

Deuterated substitutes are commonly used in neutron diffraction experiments to avoid large incoherent scattering by hydrogen, which causes high background in the diffraction patterns. Powdered $RbDCO_3$ was synthesized similar to $RbHCO_3$, but using D_2O (minimum isotope purity of 99.96 atom %D, Aldrich Chemical Co. Inc.) instead of H_2O. The initial Rb_2CO_3 powder was baked in a muffle furnace at 300 °C for 24 h to decompose $RbHCO_3$ impurities to Rb_2CO_3 ($2RbHCO_3 \rightarrow Rb_2CO_3 + H_2O + CO_2$). The purified Rb_2CO_3 was dissolved in a small amount of D_2O, and this aqueous solution was filtered through a funnel to remove undissolved impurities. The solution was placed in a vacuum desiccator under a CO_2 atmosphere for several days, and $RbDCO_3$ crystals precipitated from the solution. The presence of CO_3^{2-} ions in the solution was checked using a saturated $MgSO_4$ aqueous solution, which caused any remaining CO_3^{2-} ions to precipitate as $MgCO_3$. When almost all the CO_3^{2-} had been converted into DCO_3^- in the $RbDCO_3$ precipitate, the solution was desiccated under vacuum until all the water evaporated. Complete evaporation of water left high-purity $RbDCO_3$. To avoid hydrogen exchange with atmospheric moisture, $RbDCO_3$ was stored in a vacuum desiccator.

2.2. High-pressure experiments using diamond anvil cells (DACs)

Samples were loaded in clamped DACs, consisting of type Ia diamond anvils with a culet diameter of 600 μm. Stainless steel (SUS 301) gaskets were pre-indented to a thickness of ca. 120 μm and a 300-μm-diameter hole was drilled in the center of the gaskets. A 4:1 methanol/ethanol mixture was used as a pressure-transmitting medium. To reduce the risk of isotope substitution by the pressure-transmitting medium, a deuterated alcohol mixture of dry CD_3OD (*d*4-MeOD) and C_2D_5OD (*d*6-EtOD) (isotope purity of 99.8 atom %D) was used for $RbDCO_3$. The hydrogenated and deuterated alcohol mixtures were kept dehydrated using molecular sieves (pellet, Type-3A). The pressure was determined from several small ruby balls (several microns in diameter) using ruby

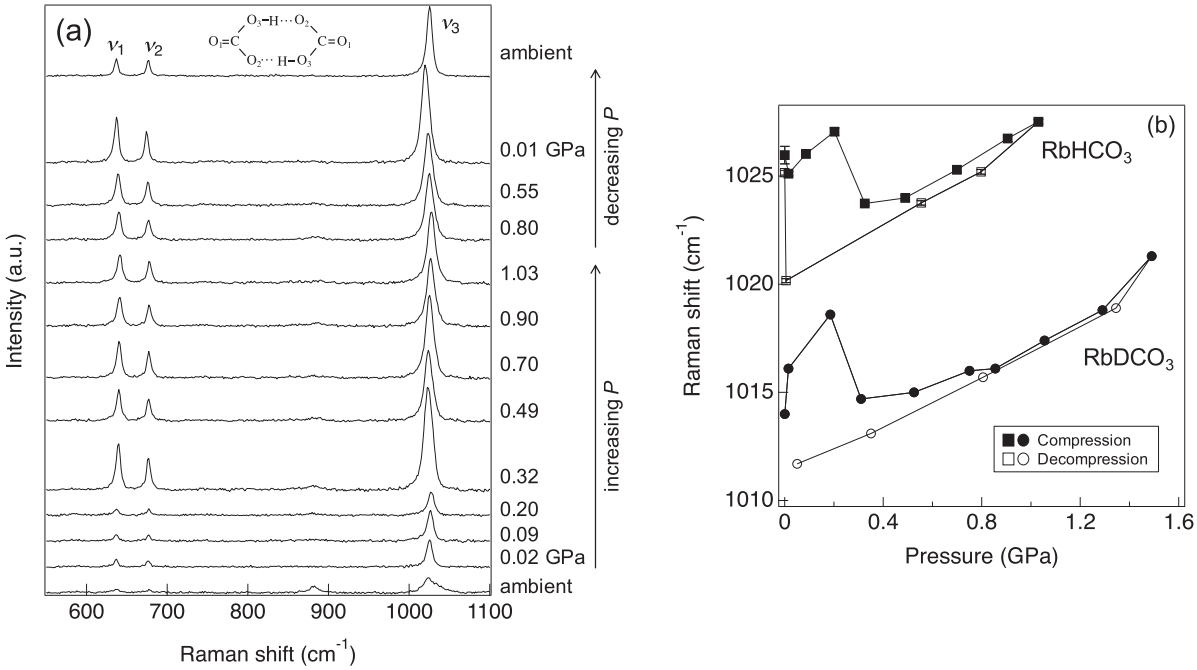

Fig. 1. **(a)** Raman spectra of $RbHCO_3$ under increasing pressure. Three bands derived from HCO_3 vibrations in $(HCO_3^-)_2$ dimers appeared in the range 600–1100 cm^{-1}: 637 cm^{-1} (δ OCO (ν_1), C–O_2 stretching and in-plane C═O bending), 676 cm^{-1} (δ OCO (ν_2), combined in-plane O_2–C–O_3 bending), and 1037 cm^{-1} (ν_3, combined C═O_1 stretching and C–O_3 stretching). **(b)** Raman shift of peak ν_3 for $RbHCO_3$ and $RbDCO_3$ vs. pressure.

fluorescence techniques [13].

2.3. Raman spectroscopy

Raman spectra at frequencies corresponding to the samples' vibration modes (500–1200 cm^{-1}) were measured at room temperature using a micro-Raman spectrometer housed at the Geochemical Research Center (GCRC), the University of Tokyo. The instrument consisted of a 50 cm single polychromator (500is, Chromex; 1200 grooves/mm diffraction grating, wavenumber resolution of 1.5 cm^{-1}/pixel), a 514.5 nm Ar^+ laser (543AP-A01, Melles Griot), and a Si-based charge-coupled device camera (DU-401A-BR-DD, Andor Technology; 1024 × 128 pixels) electrically cooled to −65 °C. The laser power was 5 mW for measuring samples and 0.2 mW for ruby fluorescence.

2.4. Synchrotron XRD

Angular-dispersive synchrotron XRD patterns of powder samples were obtained at the BL-18C beamline of the photon factory at the High Energy Accelerator Research Organization (KEK), Tsukuba, Japan. A monochromatized incident X-ray beam with an energy of ~20 keV (ca. 0.6 Å wavelength) was collimated to a diameter of 100 μm. Diffracted X-ray patterns were recorded on an imaging plate (IP) with typical exposure times of 10–20 min. The 2D diffraction image on the IP was converted into an intensity–2θ diffraction pattern using IPAnalyzer [14]. All the XRD profiles were fitted by Le Bail method using a symmetric pseudo-Voigt function with PDIndexer [14].

2.5. Powder neutron diffraction

Powder neutron diffraction patterns of $RbDCO_3$ were obtained at high pressure using a two-column Paris–Edinburgh press (type-VX4, maximum load of 200 t [15]). Single toroidal opposed anvils made of WC (diameter, 6 mm) and Ti–Zr capsulated gaskets were used for the anvil-cell assembly. The sample was loaded with a 4:1 deuterated *d*4-MeOD and *d*6-EtOD mixture as a pressure-transmitting medium. *In situ* powder neutron diffraction experiments at up to ~5 GPa were performed at beamline BL-11 (PLANET) [16], Material and Life Science Experimental Facility (MLF), Japan Proton Accelerator Research Complex (J-PARC), Tokai, Japan. A focusing mirror for incident neutrons was used and radial collimators were attached in front of the two perpendicular detector banks to reduce background. The diffraction patterns were measured by the time-of-flight method using a pulsed neutron beam. Measurement was typically for ~7 h at an accelerator power of around 400 kW. The obtained *d*-spacing was doubled in a long-wavelength frame setting (0.2–8.4 Å). Pressures were estimated from the volumetric compressibilities of $RbHCO_3$ and $RbDCO_3$ obtained from *in situ* XRD experiments at high pressure. Pressure uncertainties were estimated within ±0.1 GPa. Sample data were normalized by vanadium data to correct the energy profile of the incident neutron beam, detector sensitivity, and cell attenuation. Empty-cell data were subtracted from the individual data.

The crystal structures and atomic positions including deuterium were refined by the Rietveld technique [17] using the GSAS program [18]. The initial structure models of $RbDCO_3$ were taken from Larvor and Stöger [10] for the ambient phase ($C2/m$) and Komatsu et al. [7] for the high-P phase ($P12_1/c1$), where the unit cell parameters were slightly changed with reference to the compression data to allow consideration of the difference in pressure. Rietveld analyses were processed with individual constraining isotropic atomic displacement parameters U_{iso} for Ca, O, and D atoms. The *d*-ranges for the refinements were from ~0.6 to ~4.2 Å.

3. Results and discussion

3.1. $RbHCO_3$

3.1.1. Raman spectra

Fig. 1 shows the Raman spectra for $RbHCO_3$ during compression and decompression. At ambient pressure, the region of 600–1100 cm^{-1} contained three characteristic peaks derived from HCO_3 vibration modes in $(HCO_3^-)_2$ dimers: 637 cm^{-1} (ν_1) for C–O_2 stretching and in-plane C═O_1 bending, 676 cm^{-1} (ν_2) for combined in-plane O_2–C–O_3

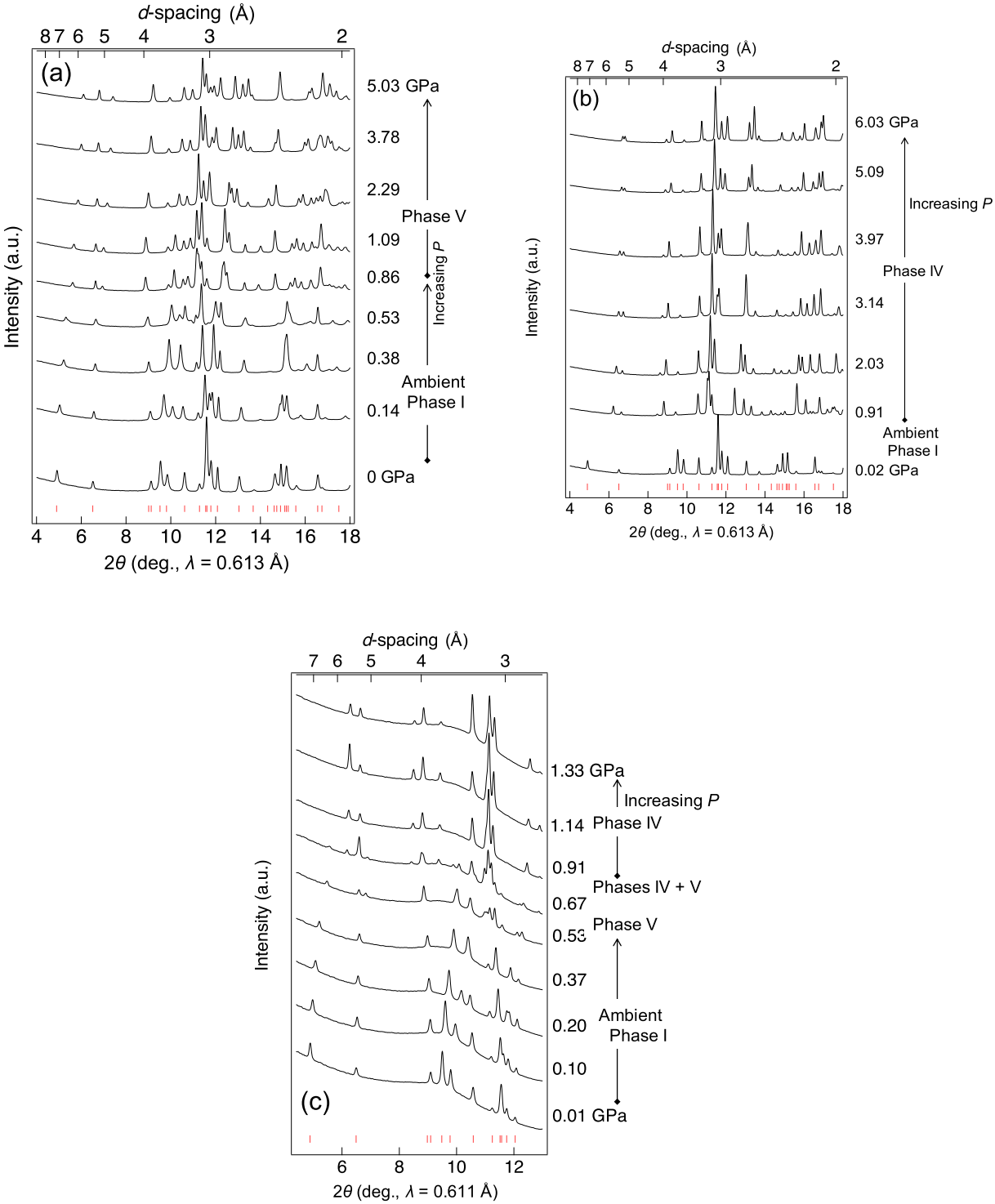

Fig. 2. Representative XRD patterns of $RbHCO_3$ under high pressure. High-P phases emerge through one of three phase transitions: **(a)** phase V, **(b)** phase IV, and **(c)** coexistence of phases IV and V. Tick marks below the patterns show the peak positions for the ambient phase I at ambient condition. Wavelength of X-ray was λ = ~0.61 Å.

bending, and 1037 cm^{-1} (ν_3) for the combination of C═O_1 stretching and C–O_3 stretching (Fig. 1a). With increasing pressure, the most intense peak, ν_3, gradually shifted to higher frequency, but dropped discontinuously from 1027 to 1024 cm^{-1} between 0.2 and 0.32 GPa (Fig. 1b). The other two peaks showed similar pressure responses to ν_3. The discontinuous drops in the vibrational modes corresponded to changes in the structure and orientation of the dimers, which was also supported by the XRD results described in Section 3.1.2. Further increases in pressure caused the frequencies of the three Raman peaks to increase monotonically. During decompression, the frequencies decreased continually, and ν_3 became 1020 cm^{-1} near 0 GPa, which was much lower than the initial value of 1026 cm^{-1}. After the DAC was opened and left at ambient conditions for several hours, ν_3 returned to 1026 cm^{-1}, indicating that the back transition occurred with a large pressure hysteresis. $RbDCO_3$

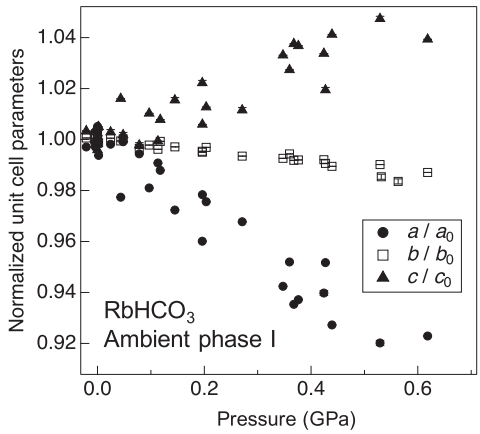

Fig. 3. Pressure dependence of normalized unit cell parameters, the ratios a/a_0, b/b_0, and c/c_0 in $RbHCO_3$ ambient phase I calculated from powder XRD results. The a_0, b_0, and c_0 are the cell parameters at ambient condition.

behaved almost identically, suggesting there were no H–D isotope effects on the pressure response (Fig. 1b).

3.1.2. XRD

$RbHCO_3$ transformed into high-P phases above about 0.5 GPa. There were two high-P phases, and the phase transition occurred in the following ways (Fig. 2): (i) a transition to a triclinic phase, (ii) a transition to a monoclinic phase, and (iii) an initial transition to the triclinic phase and a subsequent transition to the monoclinic phase through the coexistence of these two phases. Fig. 2a shows XRD patterns for transition (i). The patterns between 0.1 MPa and 0.53 GPa showed the continuous compression of ambient phase I regardless of apparent changes due to anisotropic compressibility. At 0.86 GPa, several new peaks appeared, and $RbHCO_3$ underwent a phase transition to a triclinic phase with cell parameters at 0.86 GPa of $a = 6.875(5)$ Å, $b = 5.708(3)$ Å, $c = 4.354(4)$ Å, $\alpha = 93.45(6)^\circ$, $\beta = 101.64(11)^\circ$, and $\gamma = 110.27(4)^\circ$. This structure was isostructural with the high-P phase V of $KHCO_3$ reported by Allan et al. [8], and was stable up to 5 GPa. In transition (ii), a similar change in the diffraction pattern was observed above about 0.9 GPa, but below 8° only two peaks appeared (Fig. 2b) instead of the three peaks seen in phase V (Fig. 2a). This indicated the formation of a different phase with a diffraction pattern that matched that of the monoclinic high-P phase IV of $KHCO_3$ reported by Komatsu et al. [7]. The cell parameters at 0.9 GPa after the phase transition were $a = 4.373(3)$ Å, $b = 10.594(1)$ Å, $c = 6.809(5)$ Å, and $\beta = 101.65(5)^\circ$. This high-P phase IV of $RbHCO_3$ remained stable up to 6 GPa. In transition (iii) (Fig. 2c), $RbHCO_3$ underwent the first phase transition to phase V at 0.44–0.53 GPa, and then the two high-P phases V and IV coexisted. Above 0.91 GPa, a second transition led to a single phase (phase IV), which remained stable under further compression.

In more than 15 subsequent experiments, we sought to clarify the factors controlling the formation of the different high-P phases; the conditions we varied included the starting material (powder or single crystal), pressure-transmitting material (alcohol mixture, helium gas, or a fluorocarbon fluid), and compression speed. However, no clear dependence on these factors was observed.

Fig. 3 displays the pressure dependence of the cell parameters of ambient phase I of $RbHCO_3$. Increasing pressure compressed both the *a*- and *b*-axes and elongated the *c*-axis. This anomalous elongation of the *c*-axis was not observed in the ambient phase of $KHCO_3$ (phase II) [4]. The ambient phase I of $RbHCO_3$ is isostructural to the high-T phase of $KHCO_3$ (phase I), which has disordered $(HCO_3^-)_2$ dimers [10] that may affect the high-P behavior. In the ambient phase I of $RbHCO_3$, the stacked layers of disordered dimers along the *c*-axis may be affected strongly by changes in the dimer orientation and hydrogen bonding geometry. In addition, Rb^+

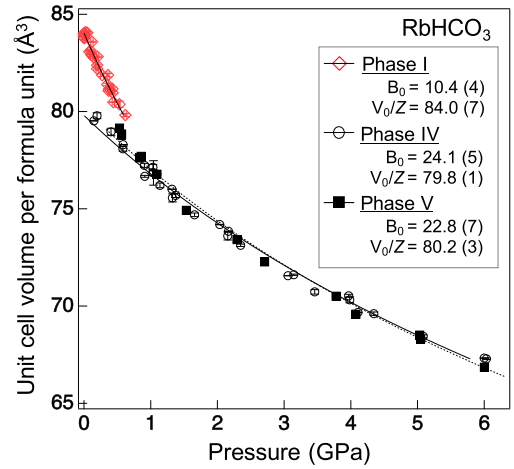

Fig. 4. Unit cell volume versus pressure in ambient phase I and high-P phases IV and V $RbHCO_3$ obtained by powder XRD. Error bars are smaller than the symbols.

Table 2
Results of Birch–Murnaghan fitting.

Phase		B_0	B'	V_0/Z	Refs.
$KHCO_3$	Phase II (ambient)	22.7(3)	4	77.78(3)	Nagai et al. [4]
$KDCO_3$	Phase II (ambient)	22.7(8)	4.1(5)	76.81(6)	Allan et al. [8]
	Phase V (high-P)	26.5(2.8)	5.2(6)	72.5(5)	Allan et al. [8]
$RbHCO_3$	Phase I (ambient)	10.4(4)	4 (fixed)	84.0(7)	This study
	Phase IV (high-P)	24.1(5)	4 (fixed)	79.8(1)	This study
	Phase V (high-P)	22.8(7)	4 (fixed)	80.2(3)	This study
$CsHCO_3$	Phase I (ambient)	22.5(6)	4 (fixed)	90.0(2)	This study

(larger than K^+) ions are arranged in Rb–O polyhedra by sharing O–O edges along the *c*-axis, and their mutual repulsion results in the elongation of this axis as shown later in Fig. 6c.

Fig. 4 shows changes of the unit cell volumes of the three $RbHCO_3$ polymorphs (phases I, IV, and V) with increasing pressure. The bulk modulus B_0 was estimated by fitting to the Birch–Murnaghan equation of state [19]:

$$P(V) = 3B_0/2\ [(V_0/V)^{7/3} - V_0/V)^{5/3}]\ \{1 + 3/4(B_0' - 4)\ [(V_0/V)^{2/3} - 1]\}, \quad (1)$$

where P is pressure, V is volume, and V_0 is the volume at ambient conditions. The fitting parameter B_0' was fixed as 4.

The B_0 and V_0 values obtained for $RbHCO_3$ are listed in Table 2 along with those for $KHCO_3$ from previous studies. $RbHCO_3$ ambient phase I has $B_0 = 10.4(4)$ GPa and $V_0 = 84.0(7)$ Å^3. Its two high-P phases IV and V showed similar values for B_0 (24.1(5) and 22.8(7) GPa, respectively) and V_0 (79.8(1) and 80.2(3) Å^3, respectively). The ambient phase was more compressible than the high-P phases, even though the fitted data points were within a narrow pressure region. Allan et al. [8] reported that phase V of $KHCO_3$ had $B_0 = 26.5(2.8)$ GPa (B_0' = 5.2(6)), which is consistent with the current results for the high-P $RbHCO_3$ phases; there are no data for high-P phase IV of $KHCO_3$.

Fig. 4 shows that the unit cell volumes (per formula unit) of $RbHCO_3$ phase IV and V remain similar throughout the pressure range considered here. This result suggests that these two phases are energetically very close, which may lead to non-unique phase transitions and their coexistence. Although it was difficult to judge which of the two high-P phases

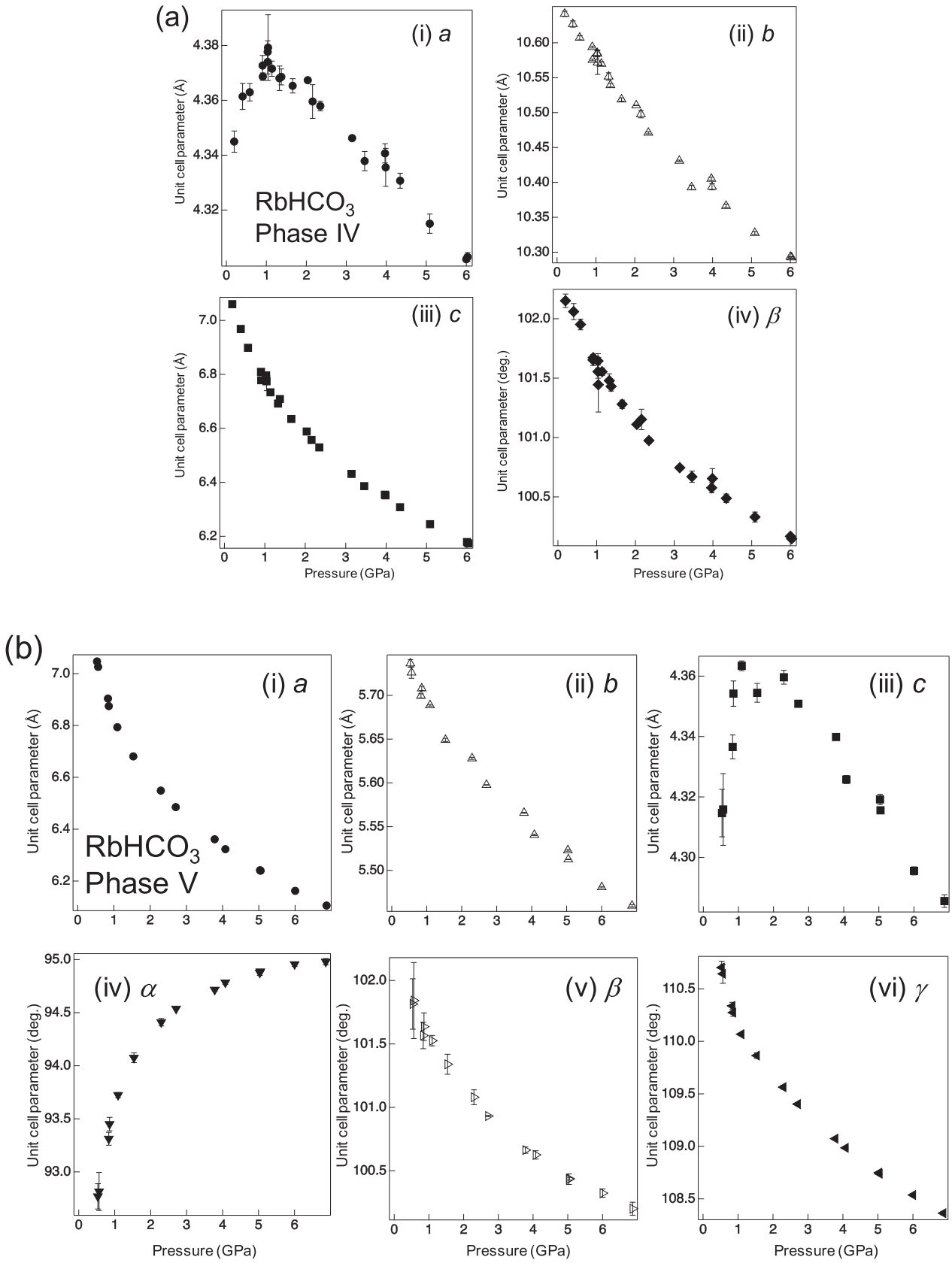

Fig. 5. Pressure dependence of unit cell parameters obtained by powder XRD **(a)** for high-P phase IV of $RbHCO_3$ (i) *a*, (ii) *b*, (iii) *c*, and (iv) β and **(b)** for high-P phase V of $RbHCO_3$ (i) *a*, (ii) *b*, (iii) *c*, and angles (iv) α, (v) β, and (vi) γ.

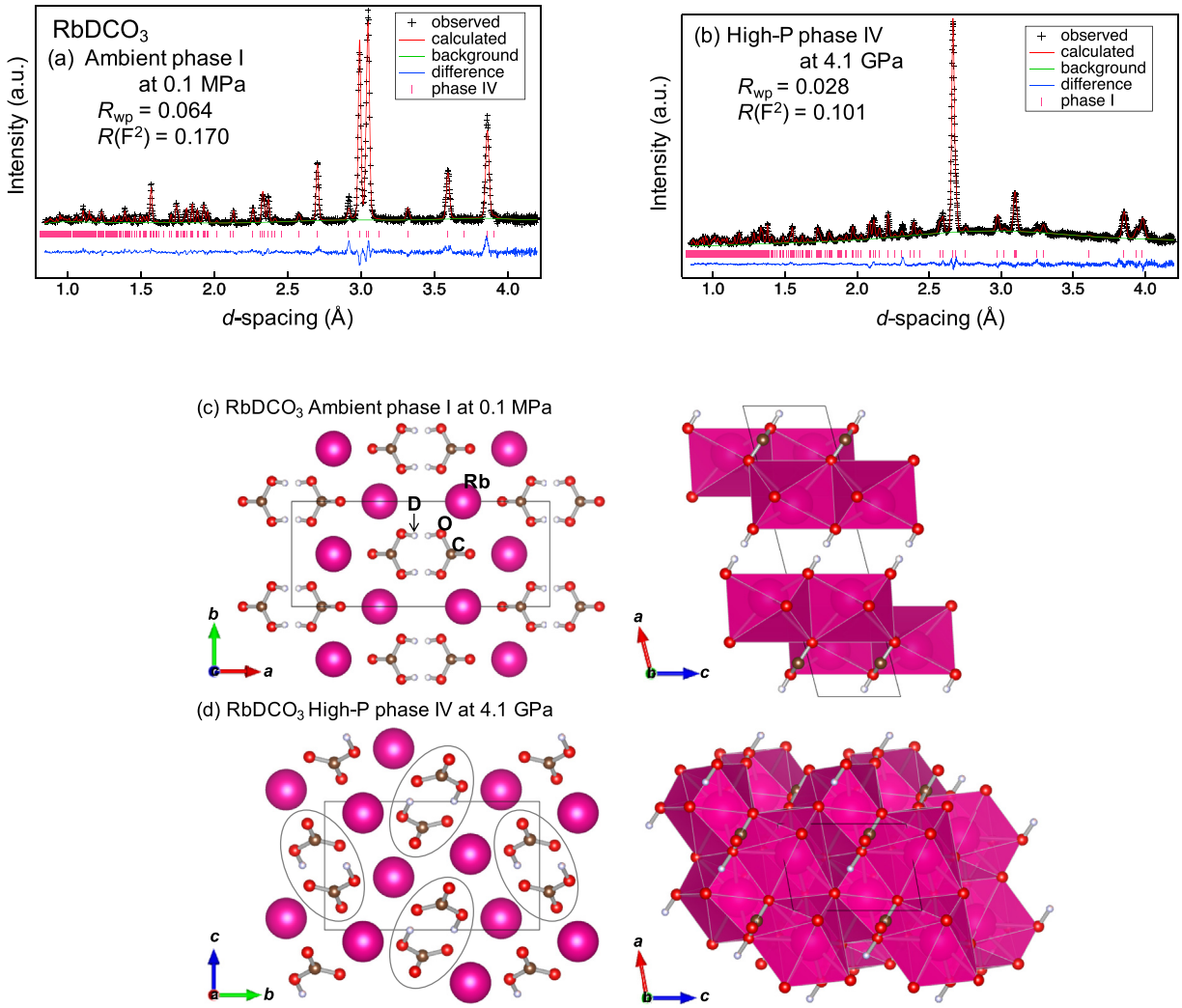

Fig. 6. Neutron diffraction patterns of $RbDCO_3$ **(a)** ambient phase I at 0.1 MPa and **(b)** high-P phase IV refined at 4.1 GPa. "+" denotes the observed data points; the solid line red denotes the calculated profile. The difference between the observed (black +) and the calculated (red) profiles is shown at the bottom of each plot. Tick marks below the pattern show the positions of allowed diffraction peaks for the corresponding phases. Crystal structures of **(c)** ambient phase I and **(d)** high-P phase IV drawn using VESTA by Momma and Izumi [21]. (For interpretation of the references to colour in this figure legend, the reader is referred to the Web version of this article.)

was thermodynamically more stable, the phase transition from phase V to phase IV was observed frequently (Fig. 2c), whereas no reverse transition was observed. This result suggests that phase IV was more stable than phase V, which is consistent with the fact that $CsHCO_3$ is isostructural with phase IV even at ambient pressure.

The axial compression of the two high-P phases of $RbHCO_3$ showed unusual behavior. The *a*-axis of phase IV (Fig. 5a) and the *c*-axis of phase V (Fig. 5b) expanded with compression at low pressure. With further compression, both axes started to shrink from the maximum, whereas all the other axes showed only continuous monotonic decreases. The unusual behavior was observed in different axes in the two phases because their different space groups use different notation. However, in each structure, these axes were oriented in the same structural direction along the layers of stacked dimers. The *a*- and *c*-axes of each high-P phase can be exchanged via a transformation matrix. These unusual axial behaviors may be related to structural changes in Rb–O polyhedra, the ordered dimer configuration, hydrogen bonding geometry, and the repulsion of Rb^+ in each structure, even after completing the phase transition (discussed later in Section 3.1.3).

3.1.3. Hydrogen bonding in high-P phase IV: Powder neutron diffraction measurements

Powder neutron diffraction at ambient conditions confirmed the synthesis of deuterated $RbDCO_3$ with a D:H occupancy ratio of approximately 4:1. Fig. 6a–b shows representative diffraction patterns of ambient phase I at 0.1 MPa and high-P phase IV at 4.1 GPa, respectively. Their crystal structures including deuterium positions were refined by Rietveld analysis (Fig. 6c–d). Table 3 lists the crystallographic data at each pressure. The neutron experiments consistently found phase IV as a high-P phase even under different conditions, such as using pellet or powdered samples, the amount of pressure medium, compression speed, and heating the sample to 80 °C to anneal the internal stress.

Fig. 7 shows the pressure dependence of the distance between Rb^+ and a neighboring O atom (*d*(Rb–O)). One Rb^+ was coordinated to eight oxygen atoms from six HCO_3^- anions in ambient phase I, and *d*(Rb–O) was 2.873(10)–3.067(3) Å. However, in high-P phase IV of $RbDCO_3$, *d*(Rb–O) varied widely between 2.872(9) and 3.483(8) Å at 0.2 GPa just after the phase transition, indicating that the Rb–O polyhedra were distorted if Rb^+ coordinated to 10 oxygen atoms. This phase IV at 0.2 GPa has still more stable Rb–O polyhedra with 9 coordinates rather than 10. The

Table 3
Crystallographic data for $RbDCO_3$ obtained by neutron diffraction.

Pressure (GPa)	0	0.04	0.15	0.58	1.32	2.17	3.06	4.11
Phase	I	I	IV	IV	IV	IV	IV	IV
a (Å)	14.8221(8)	14.4527(7)	4.3653(3)	4.3849(2)	4.3828(2)	4.3710(2)	4.3485(2)	4.32961(19)
b (Å)	5.8289(3)	5.8097(2)	10.6536(5)	10.6330(4)	10.5733(4)	10.5116(4)	10.4337(5)	10.3730(4)
c (Å)	4.0337(2)	4.0796(2)	6.9947(3)	6.8604(3)	6.6922(6)	6.5491(2)	6.4224(2)	6.3106(2)
α (°)	90	90	90	90	90	90	90	90
β (°)	104.384(4)	103.931(3)	102.040(3)	101.730(3)	101.334(3)	100.968(3)	100.690(3)	100.409(3)
γ (°)	90	90	90	90	90	90	90	90
V (Å^3)	337.57(3)	332.47(3)	318.15(3)	313.18(2)	304.07(2)	295.41(2)	286.34(2)	278.75(2)
Rb								
x	0.6637(4)	0.6627(3)	0.1522(12)	0.1491(9)	0.1432(9)	0.1493(9)	0.1517(7)	0.1530(8)
y	0	0	0.6741(5)	0.6727(3)	0.6736(3)	0.6760(3)	0.6764(3)	0.6792(3)
z	0.2945(15)	0.3022(9)	0.5776(7)	0.5796(6)	0.5826(6)	0.5874(6)	0.5888(5)	0.5898(6)
U_{iso} (× 100 Å^2)	2.9(2)	2.45(10)	3.26(11)	1.85(10)	1.51(10)	1.99(8)	1.16(7)	1.25(8)
C								
x	0.6143(5)	0.6145(3)	0.3643(12)	0.3715(9)	0.3770(9)	0.3768(10)	0.3761(7)	0.3802(9)
y	0.5	0.5	0.5272(5)	0.5473(3)	0.5458(3)	0.5455(3)	0.5454(3)	0.5445(3)
z	0.8531(16)	0.8687(10)	0.1885(9)	0.1969(5)	0.1968(6)	0.1975(6)	0.1977(5)	0.2008(5)
U_{iso} (× 100 Å^2)	2.2(2)	2.05(10)	4.24(14)	1.45(10)	1.19(10)	1.78(9)	0.87(8)	0.77(9)
O1								
x	0.6872(5)	0.6819(3)	0.6047(13)	0.6097(10)	0.6152(10)	0.6148(10)	0.6170(9)	0.6144(11)
y	0.5	0.5	0.5788(4)	0.5802(4)	0.5812(4)	0.5810(3)	0.5802(3)	0.5796(4)
z	1.094(2)	1.1033(12)	0.3168(10)	0.3134(8)	0.3224(7)	0.3208(8)	0.3210(6)	0.3254(7)
U_{iso} (× 100 Å^2)	2.94(15)	2.41(6)	2.91(6)	2.05(7)	1.72(6)	1.96(6)	1.02(5)	1.11(5)
O2								
x	0.5810(5)	0.5765(3)	0.2895(14)	0.2861(11)	0.2879(10)	0.2918(10)	0.2994(8)	0.3055(10)
y	0.3080(10)	0.3076(5)	0.4307(5)	0.4307(4)	0.4313(4)	0.4294(4)	0.4305(3)	0.4293(4)
z	0.7441(17)	0.7366(9)	0.1645(9)	0.1667(7)	0.1620(7)	0.1562(8)	0.1586(6)	0.1539(8)
U_{iso} (× 100 Å^2)	2.94(15)	2.41(6)	2.91(6)	2.05(8)	1.72(6)	1.96(6)	1.02(5)	1.11(5)
O3								
x			0.1727(16)	0.1800(12)	0.1824(11)	0.1765(13)	0.1803(10)	0.1771(12)
y			0.6342(4)	0.6346(3)	0.6352(4)	0.6381(4)	0.6364(3)	0.6383(4)
z			0.0871(11)	0.1003(8)	0.1063(8)	0.1050(8)	0.1130(6)	0.1119(7)
U_{iso} (× 100 Å^2)			2.91(6)	2.05(8)	1.72(6)	1.96(6)	1.02(5)	1.11(5)
D								
x	0.5230(12)	0.5133(12)	−0.035(3)	−0.0187(19)	−0.0152(17)	−0.0135(15)	−0.0258(12)	−0.0237(15)
y	0.3234(13)	0.3237(10)	0.5924(9)	0.5926(6)	0.5924(6)	0.5929(6)	0.5958(5)	0.5983(5)
z	0.589(4)	0.585(3)	−0.0223(19)	−0.0112(14)	0.0017(11)	0.0047(10)	0.0043(8)	−0.0003(9)
U_{iso} (× 100 Å^2)	1.7(5)	5.7(3)	4.00(5)	1.8(4)	3.0(4)	3.1(3)	3.3(3)	2.96(19)
F (D)	0.424(8)	0.416(5)	0.664(6)	0.679(9)	0.746(11)	0.755(9)	0.784(7)	0.801(15)
F (H)	0.076(8)	0.084(5)	0.336(6)	0.321(9)	0.254(11)	0.245(9)	0.216(7)	0.199(15)
R_p	0.064	0.030	0.028	0.026	0.026	0.026	0.023	0.028
R_{wp}	0.059	0.030	0.028	0.028	0.029	0.027	0.024	0.027
$R(F^2)$	0.170	0.175	0.166	0.152	0.149	0.201	0.107	0.101
N_{obs}	358	367	641	590	577	591	552	538
Hydrogen bond								
d(O–D) (Å)	0.934(14)	0.977(14)	1.143(16)	1.128(8)	1.098(7)	1.097(9)	1.112(6)	1.099(7)
d(D···O) (Å)	1.778(19)	1.610(17)	1.355(17)	1.437(8)	1.476(7)	1.473(8)	1.458(6)	1.443(6)
d(O···O) (Å)	2.701(15)	2.561(9)	2.492(14)	2.548(7)	2.552(7)	2.552(9)	2.556(6)	2.531(7)
angle(O–D···O) (°)	166.(4)	163.4(13)	172.1(13)	166.5(7)	164.9(7)	166.4(8)	167.9(5)	169.1(6)
d(Rb–O) (Å)								
Rb1–O1	2.873(10)	2.882(6)	2.872(9)	2.853(6)	2.785(6)	2.811(7)	2.808(5)	2.808(6)
Rb1–O1	3.012(8)	3.0464(16)	2.933(6)	2.928(6)	2.918(5)	2.905(6)	2.881(4)	2.883(5)
Rb1–O1	3.0669(27)	3.0464(16)	3.125(7)	3.101(6)	3.065(6)	3.001(6)	2.963(4)	2.931(5)
Rb1–O1	3.0669(27)	3.093(5)	3.149(7)	3.144(6)	3.111(6)	3.106(7)	3.058(5)	3.008(6)
Rb1–O2	2.881(8)	2.947(5)	2.935(7)	2.936(6)	2.948(6)	2.905(6)	2.852(5)	2.830(6)
Rb1–O2	2.881(8)	2.947(5)	3.109(7)	3.038(5)	2.998(5)	2.968(6)	2.984(5)	2.997(6)
Rb1–O2	3.019(7)	2.993(4)	3.257(7)	3.265(6)	3.224(6)	3.183(7)	3.119(5)	3.038(6)
Rb1–O2	3.019(7)	2.993(4)	4.021(7)	3.962(6)	3.948(6)	3.931(8)	3.909(5)	3.922(5)
Rb1–O2(O3)	3.986(10)	3.971(6)	2.927(7)	2.926(6)	2.885(7)	2.862(8)	2.857(5)	2.820(6)
Rb1–O2(O3)	3.986(10)	3.971(6)	3.050(7)	3.082(6)	3.091(6)	3.044(7)	2.999(5)	2.939(6)
Rb1–O3			3.483(8)	3.343(6)	3.251(7)	3.192(8)	3.109(5)	3.066(6)
Rb1–O3			3.565(9)	3.570(7)	3.499(7)	3.413(8)	3.372(5)	3.305(6)
Average (Å)	2.977(13)	2.993(8)	3.084(7)	3.062(6)	3.028(6)	2.998(7)	2.963(5)	2.932(6)

Note: Errors in calculated pressures are within ±0.1 GPa. U_{iso}, isotropic atomic displacement parameters; F, site occupancy; R_{wp}, R_p and $R(F^2)$, reliability factors; N_{obs}, total number of observations. Average Rb–O distances were calculated for eight (ambient phase I) and 10 (high-P phase IV) coordinates.

distance between Rb and the 10th coordinated oxygen (Rb–O3 in Table 3) for phase IV is drastically decreasing compared to other shorter Rb–O distances. Above 0.6 GPa, the coordination number of 10 is getting more stable with less variation in d(Rb–O) as the pressure increased. This gradual increase in the coordination from 9 to 10 might be caused by a rearrangement of Rb–O polyhedra to diminish the structural distortion, which also accompanies the unusual increase and decrease in the a-axis of phase IV (and the c-axis of phase V) as described above (Section 3.1.2). This suggests that complementary changes in all of the unit cell parameters result in the monotonous compression of volume for the two high-P phases shown in Fig. 4.

At 4.1 GPa, Rb^+ was more effectively coordinated to 10 oxygen atoms with d(Rb–O) ranging from 2.808(6) to 3.066(6) Å. The average d(Rb–O) did not change substantially between ambient phase I and high-P phase

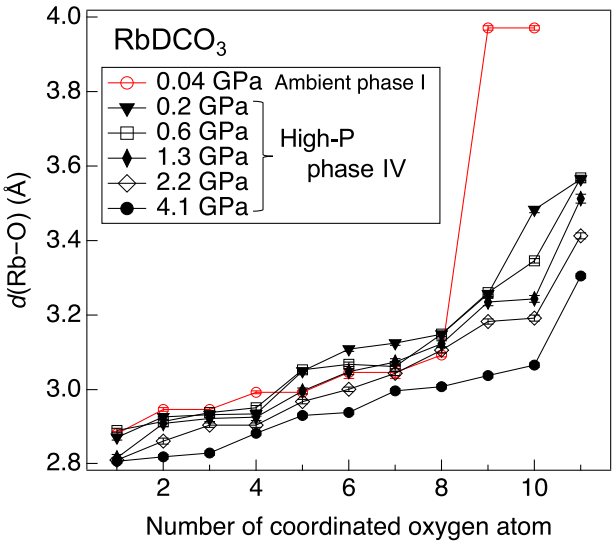

Fig. 7. Change in Rb–O distance of $RbDCO_3$ under high pressure.

IV at 4.1 GPa, despite the increase in coordination number (Table 3). This result agreed well with the increase in coordination number and the unchanging K–O distance in high-P phase V of $KDCO_3$ reported previously reported by Allan et al. [8]. Thus, the local maximum for the *a*-axis at ~1 GPa in Fig. 5a possibly resulted from the change in the configuration of the ordered $(HCO_3^-)_2$ dimer and rearrangement of the Rb^+ cations along this specific axis in high-P phase IV of $RbDCO_3$.

Fig. 8 depicts the pressure dependence of the O–D, D···O, and O···O distances and the O–D···O angle of hydrogen bonding in high-P phase IV of $RbDCO_3$. The results under ambient conditions agreed well with those of Larvor and Stöger [10]. There are no comparable data for high-P phase IV of $KHCO_3$, but data for high-P phase V of $KDCO_3$ [8] are also plotted in Fig. 8. The O···O distance in high-P phase IV of $RbDCO_3$ did not decrease, similar to that in high-P phase V of $KDCO_3$ (Fig. 8a), with no discontinuity around the phase transition at 0.2 GPa. The O–D distance became longer than that of ambient phase I just after the phase transition, and then remained mostly unchanged as the pressure increased further. Conversely, the D···O distance became shorter, and then did not change greatly or decreased slightly above ~1 GPa (Fig. 8b and c). The O–D···O angle of $RbDCO_3$ also showed no notable change at the phase transition, and then gradually increased after a local minimum at ~1 GPa; however, Allan et al. [8] reported a discontinuity for high-P phase V of $KDCO_3$ (Fig. 8d).

Jeffery [20] described the strength of hydrogen bonding in terms of bond lengths, angles, and other criteria. Strong hydrogen bonds are generally considered to have an O(–H)···O distance of 2.2–2.55 Å and an O–H···O angle of 175–180°; longer distances and angles deviating further from linear (180°) denote weaker hydrogen bonds. $KHCO_3$ has moderately strong hydrogen bonds with short O–H···O distances of ~2.6 Å even at ambient pressure [5]. The O–D···O angle in $RbDCO_3$ remained almost constant around 165°–170° after the phase transition (Fig. 8d). High-P phase IV of $RbDCO_3$ had an ordered configuration of the $(DCO_3^-)_2$ dimers, with longer O–D and shorter D···O distances than the ambient phase (Fig. 8b and c), indicating that deuterium atoms gradually moved from the donor O to the acceptor O with increasing pressure. However, the relatively short O···O distances at ~2.55 Å for ambient phase I and high-P phase IV (Fig. 8a) suggested moderately strong hydrogen bonding. Overall, the geometry of hydrogen bonding in the dimer did not change, and thus might not trigger the phase transition, although the originally disordered dimer configuration spontaneously becomes ordered.

After the phase transition, the parameters (except for the O···O distance) showed anomalous changes with a local maximum (or minimum) at ~1 GPa, which was strongly related to the unique compression behavior of the *a*-axis in phase IV (Fig. 5a). Rb^+ cations in the crystal structure were rearranged to relax the Rb–Rb repulsion as the coordination number gradually increased. The simultaneous reconfiguration of the dimers and hydrogen bonding may allow the hydrogen atoms to occupy more stable locations in the ordered dimers to enhance the geometrical stability of high-P phase IV.

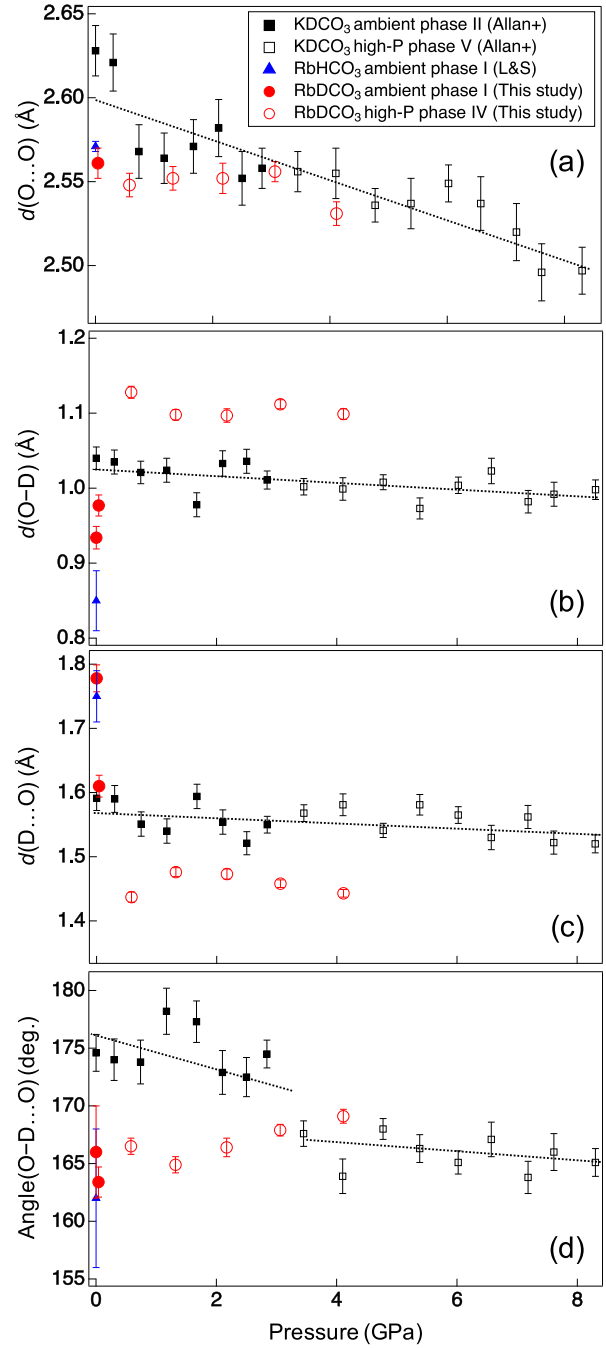

Fig. 8. Parameters of hydrogen bonding in $RbDCO_3$ vs. pressure: distances **(a)** O···O, (**b**) D–O, (**c**) D···O, and **(d)** angle O–D···O. Data for high-P phase V $KDCO_3$ are from Allan et al. [8] and those for ambient phase I of $RbHCO_3$ are from Larvor and Stöger [10]. The data points for 0.2 GPa just after the phase transition are not plotted because of the coexistence of ambient and high-P phases.

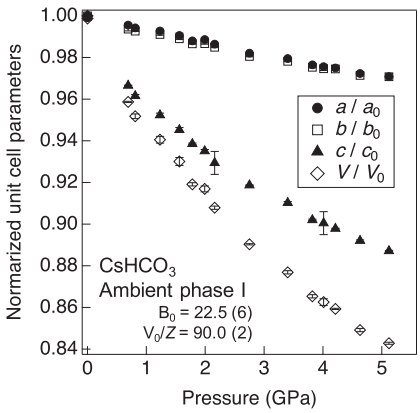

Fig. 9. Compressibility of unit cell parameters of $CsHCO_3$, ratios a/a_0, b/b_0, c/c_0, and V/V_0, calculated from powder XRD results. The a_0, b_0, c_0 and V_0 are values at ambient condition.

3.2. $CsHCO_3$

3.2.1. Raman spectra

The Raman spectra of $CsHCO_3$ (Supplementary Fig. 1a) were similar to those of $RbHCO_3$, and all the peaks shifted monotonically to higher frequency with increasing pressure (Supplementary Fig. 1b). Unlike $RbHCO_3$, there was no discontinuity observed up to 5 GPa, suggesting that no phase transition occurred in this pressure region.

3.2.2. XRD

All reflections in the XRD patterns of $CsHCO_3$ (Supplementary Fig. 2) gradually shifted to higher angles under pressures up to 5 GPa, and they were all well explained by a structure similar to phase IV $KHCO_3$ or $RbHCO_3$. Therefore, the ambient phase of $CsHCO_3$ (designated here as phase I) was stable at least up to 5 GPa. The changes in volume and cell parameters are summarized in Fig. 9 and listed in Supplementary Table 1. The bulk modulus and zero-pressure volume obtained by fitting the equations of state were $B_0 = 22.5(6)$ GPa and $V_0 = 90.0(2)$ Å^3 (Table 2).

All the axes of $CsHCO_3$ were compressed monotonically with no unusual expansions, unlike high-P phase IV of $RbHCO_3$ (Fig. 5a), despite them both having the same crystal structure. $CsHCO_3$ phase I which is isostructural to $KHCO_3$ and $RbHCO_3$ high-P phase IV, already exists stably at ambient condition.

4. Conclusions

The high-P behaviors of two alkali metal hydrogen carbonates, $RbHCO_3$ and $CsHCO_3$, were investigated and compared with previous results for $KHCO_3$. $RbHCO_3$ transformed into high-P phases at about 0.5 GPa, whereas no phase transition was found in $CsHCO_3$ up to 5 GPa. This demonstrated the effect of cation size on these compounds' high-P behaviors. Increasing the cation radius decreased the phase transition pressure, from ~3 GPa for $KHCO_3$ to ~0.5 GPa for $RbHCO_3$, with $CsHCO_3$ assuming a structure similar to the high-P form of $KHCO_3$ (monoclinic phase IV) even at ambient conditions. At high-P, phase IV (monoclinic) and phase V (triclinic) of $RbHCO_3$ with crystal structures analogous to high-P phases of $KHCO_3$ emerged. However, no thermodynamic factor was identified that determined which phase appeared and remained stable above the phase transition pressure. Although the volume and compression behavior of these two phases in $RbHCO_3$ were similar, a phase transition from phase V to phase IV or their coexistence was observed, but no reverse transition from phase IV to phase V was observed. Therefore, it is likely that phase IV is stable, while phase V is metastable. Deuterium positions in the high-P phase IV of $RbDCO_3$ were determined for the first time. In many ionic crystals, the relative size of the cation and anion greatly affects the compression behavior and pressure-induced phase transitions. In this system, however, the disordered/ordered configuration and orientation of $(HCO_3^-)_2$ dimers, together with the cation size, are strongly involved in the phase transition. The properties and networks of hydrogen bonding inside the $(HCO_3^-)_2$ dimers did not drastically change upon phase transition.

Author contributions section

G.W., R.I.-O. and H.K. performed high-P experiments. R.I.-O., G.W. and K.K. analyzed the obtained data. G.W. prepared the synthesized samples. R.I.-O., T.Y. and H.K. wrote the manuscript.

Declaration of competing interest

The authors declare that they have no known competing financial interests or personal relationships that could have appeared to influence the work reported in this paper.

Acknowledgements

The authors are grateful to Drs. T. Hattori (J-PARC, JAEA) and S. Machida (CROSS) for their helpful support in the neutron diffraction experiments at J-PARC (proposal nos. 2017B0180 and 2018A0278). *In situ* X-ray experiments were performed at the Photon Factory (PF), KEK (proposal no. 2017G644). This work was supported by JSPS KAKENHI Grant Numbers JP15H05828 and JP18H05224.

Appendix A. Supplementary data

Supplementary data to this article can be found online at https://doi.org/10.1016/j.jssc.2019.121139.

References

[1] I. Nitta, Y. Tomiie, C.H. Koo, The crystal structure of potassium bicarbonate, $KHCO_3$, Acta Crystallogr. 5 (1952) 292, https://doi.org/10.1107/S0365110X52000848.
[2] R. Sass, R. Scheuerman, The crystal structure of sodium bicarbonate, Acta Crystallogr. 15 (1962) 77–81, https://doi.org/10.1107/S0365110X62000158.
[3] S. Kashida, K. Yamamoto, Structural phase transition in $KHCO_3$, J. Solid State Chem. 86 (1990) 180–187, https://doi.org/10.1016/0022-4596(90)90133-I.
[4] T. Nagai, H. Kagi, T. Yamanaka, The first observation of a pressure-induced phase transition and compression behavior of kalicinite ($KHCO_3$) at room temperature, Solid State Commun. 123 (2002) 371–374, https://doi.org/10.1016/S0038-1098(02)00383-6.
[5] H. Kagi, T. Nagai, J.S. Loveday, C. Wada, J.B. Parise, Pressure-induced phase transformation of kalicinite ($KHCO_3$) at 2.8 GPa and local structural changes around hydrogen atoms, Am. Mineral. 88 (2003) 1446–1451, https://doi.org/10.2138/am-2003-1008.
[6] H. Kagi, T. Nagai, K. Komatsu, T. Oakda, C. Wada, J.S. Loveday, J.B. Parise, Pressure response on hydrogen bonds in potassium hydrogen carbonate and sodium hydrogen carbonate, J. Neutron Res. 13 (2005) 21–26, https://doi.org/10.1080/10238160412331297782.
[7] K. Komatsu, H. Kagi, T. Nagai, T. Kuribayashi, J.B. Parise, Y. Kudoh, Single-crystal X-ray diffraction study of high-pressure phase of $KHCO_3$, Am. Mineral. 92 (2007) 1270–1275, https://doi.org/10.2138/am.2007.2392.
[8] D. Allan, W. Marshall, C. Pulham, The high-pressure crystal structure of potassium hydrogen carbonate ($KHCO_3$), Am. Mineral. 92 (2007) 1018–1025, https://doi.org/10.2138/am.2007.2336.
[9] S. Takasaka, Y. Tsujimi, T. Yagi, Shear-stress-induced phase transition in $KHCO_3$ studied by Brillouin scattering, Phys. Rev. B 65 (2002), https://doi.org/10.1103/PhysRevB.65.174102, 174102.
[10] C. Larvor, B. Stöger, The phase transition of rubidium hydrogen carbonate, $RbHCO_3$, Crystallogr. Commun. Acta Cryst. E73 (2017) 975–979, https://doi.org/10.1107/S2056989017008271.
[11] J.A. Kaduk, Crystal structure of caesium hydrogen carbonate, $CsHCO_3$, Z. für Kristallogr. - Cryst. Mater. 205 (1993) 319–320, https://doi.org/10.1524/zkri.1993.205.12.319.
[12] J.R. Rumble, CRC Handbook of Chemistry and Physics, 98th ed., Taylor & Francis, 2017.
[13] H.K. Mao, J. Xu, P.M. Bell, Calibration of the ruby pressure gauge to 800 kbar under quasi-hydrostatic conditions, J. Geophys. Res. Solid 91 (1986) 4673–4676, https://doi.org/10.1029/JB091iB05p04673.
[14] Y. Seto, Development of a software suite on X-ray diffraction experiments, Rev. High. Press Sci. Technol. 20 (2010) 269–276, https://doi.org/10.4131/jshpreview.20.269 (In Japanese).

[15] S. Klotz, G. Hamel, J. Frelat, A new type of compact large-capacity press for neutron and x-ray scattering, High Press. Res. 24 (2004) 219–223, https://doi.org/10.1080/08957950410001661963.
[16] T. Hattori, A. Sano-Furukawa, H. Arima, K. Komatsu, A. Yamada, Y. Inamura, T. Nakatani, Y. Seto, T. Nagai, W. Utsumi, T. Iitaka, H. Kagi, Y. Katayama, T. Inoue, T. Otomo, K. Suzuya, T. Kamiyama, M. Arai, T. Yagi, Nucl. Instrum. Methods A 780 (2015) 55–67, https://doi.org/10.1016/j.nima.2015.01.059.
[17] H.M. Rietveld, A profile refinement method for nuclear and magnetic structures, J. Appl. Crystallogr. 2 (1969) 65–71, https://doi.org/10.1107/S0021889869006558.
[18] A.C. Larson, R.B. Von Dreele, General structure analysis system (GSAS), Los Alamos Natl. Lab. Rep. LAUR 86 (2004) 748.
[19] F. Birch, Elasticity and constitution of the Earth's interior, J. Geophys. Res. 57 (1952) 227–286, https://doi.org/10.1029/JZ057i002p00227.
[20] G.A. Jeffrey, An Introduction to Hydrogen Bonding, Oxford University Press, Oxford, UK, 1997, pp. 119–123.
[21] K. Momma, F. Izumi, VESTA: a three-dimensional visualization system for electronic and structural analysis, J. Appl. Crystallogr. 41 (2008) 653–658, https://doi.org/10.1107/S0021889808012016.